Numerical Simulation of Solids Suspension in a Stirred Tank

J. J. Derksen
Kramers Laboratorium voor Fysische Technologie, Delft University of Technology,
Prins Bernhardlaan 6, 2628 BW Delft, The Netherlands

Large-eddy simulations of the turbulent flow driven by a Rushton turbine have been coupled to a Lagrangian description of spherical, solid particles immersed in the flow. The working fluid was water, whereas the solid particles had the properties of glass beads. Simulations were restricted to a lab-scale tank (volume 10^{-2} m^3), and relatively low solids volume fractions (up to 3.6%). Two sets of particles were considered with particle dia. of 0.30 mm and 0.47 mm, respectively. It has been investigated to what level of detail the particle motion needs to be modeled in order to meet Zwietering's just suspended criterion. It appeared to be essential to take particle-particle collisions into account, mainly because of their exclusion effect that prevents unrealistic buildup of particle concentrations closely above the bottom. The simulations give detailed insight in the behavior of the particles, and in the way that the liquid flow is altered by the presence of the particles. The frequency and intensity of particle-particle collisions, and particle-impeller collisions, have been investigated. Furthermore, it will be demonstrated that the rotational Reynolds numbers of the big (0.47 mm) particles were of the same order of magnitude as their translational counterparts.

Introduction

Turbulently agitated solid-liquid suspensions are encountered in a large variety of industrial processes. Examples are catalytic slurry reactors in which solid particles that carry catalytic material are suspended in the turbulent flow induced by an impeller. The turbulent fluid flow keeps the particles suspended, and enhances mass and heat transfer between the solid and liquid, thereby enabling reactions of chemicals contained in the continuous phase liquid. In (reactive) crystallization, solid crystalline particles are produced in stirred tanks. The product characteristics are strongly influenced by the turbulence properties in the vessel: the mass transfer needed for nucleation and growth is brought about by the fluid flow; agglomeration and attrition (a major source for secondary nucleation) are related to crystal-crystal collisions that are induced by local velocity gradients (Hollander et al., 2001), and crystal inertia. Furthermore, attrition is expected to occur due to crystal-impeller collisions, the frequency and intensity of which is the result of an intricate interplay between fluid flow and particle motion. Also, particle-coating processes may be carried out in stirred tanks, with, for example, heterogeneous reactions at the solid-liquid interface. Solid suspension in stirred tanks is also relevant for suspension polymerization processes. In such processes one usually starts off with a stirred liquid-liquid system that, during the course of polymerization reaction, turns into a solid-liquid system (Kiparissidis, 1996).

There are many unresolved issues with respect to what is actually going on at the particle scale (in terms of, for example, heat and mass transfer, mechanical load on particles as a result of particle-particle and particle-impeller collisions) and how the presence of particles influences local and global flow features in the vessel such as the vortex structure in the vicinity of the impeller, power consumption, circulation and macro-mixing times, and the distribution of turbulence quantities. Next to experiments and theoretical considerations, numerical modeling is a way to investigate these issues.

Realistic modeling of solids suspension in turbulently stirred tanks (even without heat and mass transfer, not to speak about chemical reactions) is not an easy task. With the present and foreseeable future computational resources, we will not be able to directly solve the flow system under consideration, that is, to resolve in an industrial-scale reactor all turbulent length and time scales, to resolve the entire solid-liquid interface, and to resolve in detail the particle-particle

collision and particle-wall collision events. Therefore, we need to revert to modeling. Many approaches exist to model the motion of mixtures of two phases, where one phase is dispersed in the other. Grossly speaking, they can be divided into Eulerian/Eulerian (Eu/Eu) and Eulerian/Lagrangian (Eu/La) approaches (Crowe et al., 1996). In the former approach the two phases are considered to be interpenetrating continua. It heavily relies on the modeling of the phase interaction terms that appear in the equations describing the dynamics of the system. Solid-liquid flow simulations in turbulently agitated tanks based on this approach have been reported by (among others) Montante et al. (2001). In an Eu/La approach, the disperse phase is considered in terms of individual particles for which the equations of motion are solved (see, for example, Lain et al., 2002). For the hydrodynamic forces acting on the particles, mostly single-particle correlations are applied. This limits the method to systems with relatively low dispersed phase volume fractions since hydrodynamic interactions between particles are not taken into account. By feeding back the hydrodynamic forces on the particles to the continuous phase (action-reaction), two-way coupling between the two phases is achieved. Eu/La simulations are excellently suited to study the influence of modeling assumptions regarding the phase interactions ("what if" questions): forces and other physical phenomena can be switched on and off at will.

This article is intended to assess by Eu/La simulation the relevance of some physical aspects of a turbulently agitated liquid-solid suspension. Furthermore, results with respect to particle behavior that may have practical implications are presented, such as the spatial distributions of particle concentrations, slip velocities and rotational velocities, particle-particle collision frequencies and intensities, and particle-impeller collisions. The simulations are restricted to dilute suspensions (solids volume fractions up to 3.6%), and a lab-scale vessel (with a volume of 10^{-2} m^3). In chemical engineering practice, volume fractions and equipment scales are generally much larger. In the author's opinion, however, its focus on the physical mechanisms makes this article worthwhile for chemical engineers, since these mechanisms have generic significance and, therefore, play a role in full-scale, solid-liquid processes as well.

The basis of the simulations discussed here is a representation of the continuous phase flow by means of large-eddy simulation (LES). As will be argued, this way of turbulence modeling leaves less room for speculation in modeling the turbulence and the motion of solids immersed in the flow compared to RANS-based turbulence modeling, at the expense of an increased computational effort. It has been clearly demonstrated that LES can accurately represent the single-phase flow in a stirred tank, including the turbulent fluctuation levels (Derksen and Van den Akker, 1999). In the LES flow field, spherical particles are released according to an Eu/La approach. As mentioned above, we do not resolve the fluid-solid interface at the particle surface; the size of the particles is smaller than the grid-spacing. The dynamical behavior of the particles is determined by semi-empirical correlations for the forces exerted by a (inhomogeneous) fluid flow on single particles. Forces that will be taken into account are gravity, drag, the force due to added mass, Saffman force, Magnus force, and the force due to stress gradients (pressure and viscous stress). The influence of the latter three forces, and the influence of particle-particle collisions and two-way coupling (that is, the impact the presence of particles has on the continuous phase flow) on the behavior of the two-phase system will be investigated explicitly. Since, in our Eu/La approach, the forces acting on the solid particles are based on correlations that are strictly speaking, valid only for single particles in unbounded fluid flow, the volume fractions are limited for which physically sound simulations can be done. Furthermore, the computational effort spent on particle tracking is strongly dependent on the number of particles (linearly proportional without taking into account particle-particle collisions; superlinearly proportional if particle-particle collisions are taken into account). These considerations forced us to limit the size of the tank, and the solids volume fractions applied here.

In the next section, the two-phase flow system will be defined in terms of its geometry and vessel content. In the subsequent section, the various modeling approaches will be discussed, eventually leading to an overview of the simulation cases. In the Results section, the outcome of the various cases will be compared. A major point of discussion will be the impact of the modeling assumptions on the distribution of the solids throughout the vessel. Furthermore, results on collisions (particle-particle and particle-impeller), on the properties that determine solid-liquid mass transfer, and on the (continuous phase) turbulent flow will be presented. The conclusions will be summarized in the final section.

Flow System

The stirred tank has a standard configuration. It consists of a cylindrical, flat-bottomed, baffled tank with diameter (T) equal to the liquid height. The top of the vessel is closed with a lid. The impeller that drives the flow is a Rushton turbine with diameter $D = T/3$, placed with a bottom clearance $C = D$. The geometry is defined in Figure 1. The Reynolds number (that fully determines the single-phase flow) is defined as $Re = ND^2/\nu$, with N the impeller speed (in rev/s), and ν the kinematic viscosity of the working fluid.

In order to better appreciate the agitated solid-liquid system, we will now switch to dimensional numbers. The vessel

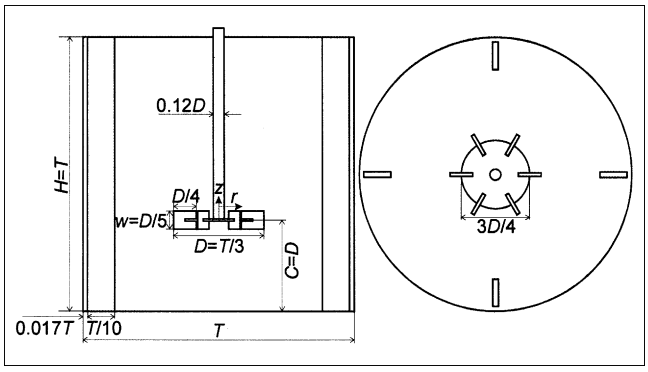

Figure 1. Flow geometry and (r,z) coordinate system.

(Left) side view, (right) top view. The vessel content is covered with a lid (no-slip wall). The thickness of the impeller blades and disk amount to $0.035D$, the thickness of the baffles to $0.02T$. The axial level with $z = 0$ is at the impeller disk.

volume was set to 10^{-2} m^3, which implies that $D = 7.78 \cdot 10^{-2}$ m. The continuous phase was water (with $\nu = 1 \cdot 10^{-6}$ m^2/s, and $\rho_l = 1 \cdot 10^3$ kg/m^3). Two sets of particles were released in the tank. The first set (particle set No. 1) consisted of 6,705,623 spherical particles with diameter $d_p = 0.30$ mm, and density ratio $\rho_p/\rho_l = 2.5$ (with ρ_p the density of the particles), typical for glass beads in water. As a result, the solids volume and mass fractions amounted to $\Phi_V = 0.95\%$ and $\Phi_m = 2.37\%$ respectively. The impeller was set to revolve with $N = 16.5$ rev/s ($Re = 1 \cdot 10^5$). The Stokes number of the particles was $Stk = 0.21$ (with $Stk = (\rho_p/\rho_l)\,(d_p^2 N/18\nu)$; the ratio of the Stokesian particle relaxation time, and the time of one impeller revolution). The impeller speed was chosen to be slightly above the just-suspended impeller speed according to the Zwietering (1958) correlation (see also Baldi et al., 1978) for this system

$$N_{js} = s\frac{d_p^{0.2}\nu^{0.1}\left(|\,\boldsymbol{g}\,|\,\Delta\rho\right)^{0.45}\Phi_m^{0.13}}{\rho_l^{0.45}D^{0.85}} = 13 \text{ rev/s}$$

($\boldsymbol{g}$ is the gravitational acceleration vector, $\Delta\rho = \rho_p - \rho_l$, and Φ_m is the solids mass fraction in %; the constant $s = 8$ for our configuration). As a consequence, the least requirement for the result of a simulation is that it shows sufficient suspension of the solids.

The second set of particles (particle set No. 2) had $d_p =$ 0.468 mm. The number of particles and the density ratio were the same as for set No. 1. The solids volume fraction was now significantly higher: 3.6%. Also, the just-suspended impeller speed increased for this system: $N_{js} = 17$ rev/s. In the simulations with the second set of particles, the impeller speed was set to $N = 25$ rev/s ($Re = 1.5 \cdot 10^5$; $Stk = 0.76$).

Aspects of Modeling

Single-phase flow

For the single-phase (that is, the Eulerian) part of the simulations, an in-house developed lattice-Boltzmann code has been employed. The features of the code that are relevant to turbulent, stirred tank flow have been documented in Derksen and van den Akker (1999). In summary, lattice-Boltzmann methods provide a second-order discretization (in space and time) of the incompressible Navier-Stokes equation on a uniform, cubic lattice (Chen and Doolen, 1998). The method has been chosen for its flexibility with which complex flow geometries can be represented, and because of its parallel efficiency. The latter is due to the locality of its arithmetic operations, as a result of which parallelization based on domain decomposition only requires communication of limited amounts of subdomain-boundary data. This implies that parallel versions of the code run efficiently on cheap PC clusters (so-called Beowulf clusters), whose only weak point is the relatively slow interconnectivity between the CPUs as compared to (expensive) supercomputers.

The Reynolds numbers that were presented in the previous section imply a strongly turbulent flow that cannot be fully resolved by the computational grid: A rough estimate of the Kolmogorov length scale η_K for the case with $Re = 10^5$ based on the scaling rule $\eta_K/L = Re^{-3/4}$ with the integral scale L taken to be D (this is an upper estimate, it may be more realistic to relate the integral scale to the impeller blade dimensions) comes down to $\eta_K = 2 \cdot 10^{-4} D$. As a result, for a full resolution of the flow of the order of 10^{12} grid nodes are required, which is beyond current computational resources. To overcome this problem, we apply large-eddy simulation (LES). For this, the full three-dimensional (3-D) geometry of the tank needs to be simulated as a function of time, since we need to be able to resolve the evolution of the large(st)-scale structures. The grid that is applied in the LES contained 240^3 (that is, $1.4 \cdot 10^7$) nodes. As a result, the linear size of the cubic lattice cells amounted to approximately 1 mm. The flow resolved by the grid can be interpreted as a low-pass filtered representation of the true flow. The impact of the fluid motion that resides at the subgrid-scales (that is, the part that has been filtered out) on the motion at the grid scales requires modeling. For this, we apply the Smagorinsky subgrid-scale (SGS) model (Smagorinsky, 1963). In the Smagorinsky model, the action of the SGS motion is considered to be purely diffusive: it is represented by an eddy viscosity ν_e according to

$$\nu_e = (c_S\Delta)^2\sqrt{S^2} \tag{1}$$

with c_S a constant (the Smagorinsky constant) set to 0.1, Δ the lattice spacing, and $\sqrt{S^2}$ the resolved deformation rate. The time step size in the LES was such that one impeller revolution took 2,800 time steps.

Results of the single-phase Lattice-Boltzmann LES code applied to stirred tank flow have been extensively compared to phase-averaged, and phase-resolved experimental data (see Derksen and van den Akker, 1999; Derksen, 2001). As long as the spatial resolution is sufficient, excellent agreement of numerical and experimental data have been reported. Global, as well as subtle, flow features, such as the path along which the trailing vortices develop in the wake of impeller blades, are swept in the bulk of the tank: the turbulent kinetic energy levels in the wake of impeller blades; the primary and secondary recirculation in the phase-averaged flow generated by a pitched-blade turbine were all predicted in quantitative agreement with experimental data. In Derksen (2001), it has been shown that choices made in SGS modeling were not very critical for the quality of the flow field results. In addition, it has been verified that the choice of the Smagorinsky constant c_S is hardly influential to the single-phase flow field when varied between $c_S = 0.08$ and $c_S = 0.14$.

In the LES flow field, solid particles are released that in general not only feel the resolved part of the fluid motion, but also the SGS part. It is desirable that the forces exerted by the fluid flow on the particles are dominated by the (known) resolved part, and not by the SGS part that is, at best, known in statistical terms (such as its variance). Since it is expected that the major fluid-flow related force acting on the particles is the drag force, the fluid's velocity field is of primary interest here (to a lesser extent, pressure and stresses are relevant). Two complementary criteria should be satisfied for the resolved flow to dominate the particle motion. In the first place, the resolved velocity fluctuations should be much stronger than the (estimated) SGS fluctuations. In the second place, the particle relaxation time should be larger than the

time-step applied in the LES. Satisfaction of the latter criterion implies that the time-step can keep up with the particle time-scale. The Stokes numbers (which have been defined above as the ratio of the particle relaxation time over the time required for one impeller revolution) applied here are of the order 1. Since $\Delta t = 1/2{,}800N$, the time-step criterion is met. In the Results section we will compare the strength of the resolved and unresolved part of the velocity field. If the two criteria are satisfied, (speculative) stochastic modeling of fluid motion that represents the SGS velocities has very little influence on the particle behavior. Since the resolved velocities are not much influenced by the choices made in the SGS modeling (as discussed above), meeting the two criteria implies that solid particle motion is also hardly influenced by the SGS modeling choices.

With a RANS-based simulation, the role of stochastic modeling for particle tracking is in general much larger than with an LES, since the velocity fluctuations in a RANS simulation are represented in statistical terms (by their second-order moments, that is, the Reynolds stresses), and only very schematically in terms of spatial and temporal correlations (such as from the turbulent kinetic energy and energy dissipation rate values, turbulent time scales can be estimated). As a result, particle tracking in a RANS field will give less realistic results than in a LES field.

Solid particle dynamics

Without much discussion, it can be anticipated that particle inertia, gravity, and drag need to be part of the equations of motion of the solid particles. Since a stirred tank flow is very inhomogeneous, it is difficult to estimate *a priori* if more exotic forces like lift and history forces play an important role. For instance, an estimate of the ratio between lift (Magnus and/or Saffman force) and drag forces is $0.2\sqrt{d_p^2|\hat{\boldsymbol{\omega}}|/\nu}$, with $|\hat{\boldsymbol{\omega}}|$ the vorticity in the liquid phase or the angular (slip) velocity of the particle. In the impeller region of single-phase stirred tank flow, vorticity easily exceeds $10N$ (Derksen and van den Akker, 1998). With $N = 16.5$ rev/s and $d_p = 0.3$ mm, the ratio amounts to 0.8, indicating the potential relevance of lift forces.

Each particle dispersed in the stirred tank has six degrees of freedom associated to it: three linear coordinates and three angles. Since we consider the particles to be spherical, the particle's orientation has no physical consequence. As will be demonstrated below, the angular velocity has physical significance. For the linear motion, the following set of equations will to be solved

$$\frac{d\boldsymbol{x_p}}{dt} = \boldsymbol{v_p} \tag{2}$$

$$\frac{\pi}{6}d_p^3\left(\rho_p + \frac{1}{2}\rho_l\right)\frac{d\boldsymbol{v_p}}{dt} = \frac{\pi}{8}d_p^2\rho_l C_D|\boldsymbol{u}-\boldsymbol{v_p}|(\boldsymbol{u}-\boldsymbol{v_p}) + \boldsymbol{F}_{\text{Saffman}} + \boldsymbol{F}_{\text{Magnus}} + \boldsymbol{F}_{\text{stress}} + \frac{\pi}{6}d_p^3(\rho_p-\rho_l)\boldsymbol{g} \tag{3}$$

with $\boldsymbol{x_p}$ the center position of the particle, $\boldsymbol{v_p}$ and $\boldsymbol{u}$ the velocity of the particle, and the velocity of the liquid at $\boldsymbol{x_p}$, respectively, and C_D the drag coefficient. The latter depends on the particle Reynolds number $Re_p = |\boldsymbol{u}-\boldsymbol{v_p}|d_p/\nu$ according to Eq. A1, given in the Appendix (Sommerfeld, 2001). The solids volume fractions are considered to be sufficiently low not to include a dependency of C_D on Φ_V. Added mass is accounted for by the additional particle inertia $\pi/12\,d_p^3\rho_l$ (Maxey and Riley, 1983). The influence of the Saffman force ($\boldsymbol{F}_{\text{Saffman}}$), Magnus force ($F_{\text{Magnus}}$), and the force due to stress gradients ($\boldsymbol{F}_{\text{stress}}$) will be discussed below where simulations with and without these forces will be compared.

The Basset history force (Odar and Hamilton, 1964) may have some impact in the impeller region, with its strong velocity fluctuations at frequencies of the order of $6N$. The ratio between the Basset history force and Stokes drag in a time-varying flow field with frequency f is of the order of $0.1\sqrt{d_p^2 f/\nu}$. If we take $f = 6N$, the ratio is 0.3 for the simulation with particle set No. 1, and 0.6 for set No. 2. It will be demonstrated, however, that in the impeller region, Re_p is of the order 10^2. As a result, the drag force is one order of magnitude higher than estimated from Stokes drag and the Basset force becomes small compared to the drag force. For this reason, and for computational reasons (inclusion of the force would add appreciably to the computational effort), the Basset force has been neglected.

The non-Stokes expressions we use for the Saffman and Magnus force, respectively, are (Mei, 1992; Oesterlé and Bui Dinh, 1998)

$$\boldsymbol{F}_{\text{Saffman}} = \frac{\pi}{4}d_p^3\frac{\rho_l}{2}C_S\big((\boldsymbol{u}-\boldsymbol{v_p})\times\boldsymbol{\omega}\big) \tag{4}$$

$$\boldsymbol{F}_{\text{Magnus}} = \frac{\pi}{4}d_p^2\frac{\rho_l}{2}C_M|\boldsymbol{u}-\boldsymbol{v_p}|\frac{(\boldsymbol{\omega}-2\boldsymbol{\omega_p})\times(\boldsymbol{u}-\boldsymbol{v_p})}{|\boldsymbol{\omega}-2\boldsymbol{\omega_p}|} \tag{5}$$

with $\boldsymbol{\omega}$ the vorticity of the liquid, and $\boldsymbol{\omega_p}$ the angular velocity of the particle. The lift coefficients C_S and C_M depend on Re_p, and on the rotational Reynolds numbers $Re_S = |\boldsymbol{\omega}|d_p^2/\nu$, and $Re_R = |1/2\,\boldsymbol{\omega}-\boldsymbol{\omega_p}|d_p^2/\nu$ according to Eqs. A2 and A3. The force due to stress gradients has a pressure and a viscous stress part

$$\boldsymbol{F}_{\text{stress}} = \frac{\pi}{6}d_p^3\big(-\nabla p + \rho_l\nu\nabla^2\boldsymbol{u}\big) \tag{6}$$

In order to determine the Magnus force (Eq. 5), the angular velocity of the particles needs to be solved. This is done by solving the following dynamic equation

$$\frac{d\boldsymbol{\omega_p}}{dt} = \frac{60}{d_p^2}\frac{\rho_l}{\rho_p}\nu\left(\frac{1}{2}\boldsymbol{\omega}-\boldsymbol{\omega_p}\right) \tag{7}$$

which is valid for $Re_R \le 30$ (Dennis et al., 1980). The particles' angular velocity may also be relevant from a practical point of view. Mass transfer between solid particles and continuous phase liquid depends on the motion of the solid surface relative to the liquid. Apart from linear velocities, particle rotation might play a role in mass exchange.

The fluid's velocity $\boldsymbol{u}$, vorticity $\boldsymbol{\omega}$, pressure p, and viscous stress $\rho_l\nu\nabla\boldsymbol{u}$ contained in the above equations all consist of a resolved and a subgrid-scale (SGS) part. For reasons of sim-

plicity, the SGS parts have been discarded, except when the drag force is involved. For determining the drag force, the local fluid velocity is considered to be the sum of the resolved velocity and a Gaussian random process with standard deviation $u_{sgs} = \sqrt{2/3 k_{sgs}}$ representing the SGS motion. The SGS kinetic energy k_{sgs} was estimated based on isotropic, local-equilibrium mixing-length reasoning according to

$$k_{sgs} = C_k c_s^2 \Delta^2 S^2 \tag{8}$$

with C_k a constant amounting to 5 (Mason and Callen, 1986). To have temporal coherency in the SGS motion, a new random velocity was picked after the elapse of a SGS eddy lifetime

$$t_{sgs} = C_L \frac{k_{sgs}}{\epsilon} \tag{9}$$

with the constant $C_L = 0.15$ (Weber et al., 1984), and ϵ the energy dissipation rate.

The resolved part of the liquid velocity was determined by linearly interpolating the velocities on the lattice-Boltzmann grid to the particle position. The vorticity, and the pressure and viscous stress gradients felt by the solid particles were taken uniform over a grid cell. The stresses are directly contained in the solution vector of the lattice-Boltzmann scheme. Their gradients, as well as the velocity gradients contained in the vorticity, were determined from central finite differencing. Note that the determination of the force due to stress-gradients differs from how it is usually done, that is, by means of the material time derivative of the fluid velocity (see, for example, Crowe et al., 1998). Since in a Lattice-Boltzmann scheme the stresses are readily available, it is not expensive to directly determine the stress gradients.

Equation 3 was time-discretized according to a first-order mixed explicit/implicit scheme. The Saffman and Magnus force on the righthand side of Eq. 3 were evaluated on the old time step, whereas the linearized drag force term was treated implicitly. Equation 7 was treated first-order implicitly. The time step in the discrete version of the three evolution Eqs. 2, 3, and 7 was equal to the time step with which the flow field was updated.

Collisions

Three types of collisions need to be distinguished: particle-wall, particle-impeller, and particle-particle collisions. Collisions of all types were considered to be fully elastic and frictionless (the latter implies that, in a particle-wall and particle-impeller collision, the wall parallel components of the velocity of the particle *surface* are unchanged after a collision; in a particle-particle collision the rotation of the particles does not play a role in the collisional process). For the particle-impeller collisions, only a collision with one of the (six) impeller blades adds momentum to a particle since only the impeller blades have a velocity component in their wall-normal direction. At the event of an impeller blade collision, the particle velocity is updated according to

$$v_{p,\theta,\text{out}} = -v_{p,\theta,\text{in}} + 2 r_p \Omega \tag{10}$$

(with $v_{p,\theta,\text{out}}$ and $\nu_{p,\theta,\text{in}}$ the tangential velocity after and before the collision, respectively, and $r_p\Omega$ the local velocity of the surface of the blade; $\Omega = 2\pi N$).

The method for detecting and handling particle-particle collisions was similar to the one proposed by Chen et al. (1998). In their method, they make use of a collision detection algorithm that anticipates collisions in the upcoming time step. Subsequently, the path of two particles that are bound to collide is integrated in a three-step-process: the pre-collision step, the collision step (in which the particles exchange momentum), and the post-collision step. In order to limit the computational effort spent in handling the particle-particle collisions (which, in principle, is an M^2 process, with M the number of particles) we have grouped the particles in each other's vicinity in a so-called link list (Chen et al., 1998). The extent of the vicinity of a particle in which potential collision partners are sought is the lattice cell in which the particle under consideration resides, and the 26 neighboring cells. The distance traveled by a particle during one time step was, at most, 0.2Δ. This reduces the number of possible collisions partners to a few for a specific particle during a specific time step.

The collision algorithm assumes that one particle can only collide once during one time step. The reason is purely practical: taking into account multiple collisions in one time step would lengthen the computations to an unfeasible extent (such as allowing for the possibility to have two collisions per particle per time step would make an M^3 process). The assumption either limits the time step or the particle volume fraction. In any case, there is a finite chance in the simulations that the collision detection algorithm misses a collision. This is reflected in the situation that, at the next time step, two approaching particles have a mutual distance less than d_p. If this occurs, a so-called missed collision procedure is executed: directly at the start of the time step, the particles involved are given their post-collision velocities (indicating that they now are moving apart). During the time step, the particles are displaced as a pair according to their average velocity, and they move apart with their relative velocity until they have a mutual separation of at least d_p.

The particle-particle collision algorithm has been tested by (numerically) releasing a set of particles with random initial velocity (according to a uniform distribution) in a periodic vacuum box. The velocity distribution should relax to a Maxwellian distribution, and it did. In the same setup, the algorithm described above to repair missed collisions was tested. Ignoring missed collisions led to one order of magnitude more overlapping particles at any moment in time compared to a situation in which the missed collision procedure was applied.

Two-way coupling

In the simulations, solids volume fractions are such that it is expected that two-way coupling effects are relevant (Elgobashi, 1994). Two-way coupling effects have been explicitly investigated by comparing cases with two-way coupling switched on and off.

Two-way coupling was achieved by feeding the force that the fluid exerts on the particle back to the fluid. Since the center position of a particle in general does not coincide with

a grid point, the back-coupling force needs to be distributed over the (lattice-Boltzmann) grid nodes in the vicinity of the particle. For this extrapolation, we used the same coefficients as were used for the linear interpolation of the velocity at the grid nodes to the particle location.

Parallelization aspects

As briefly described above, the lattice-Boltzmann method is well suited for parallelization. In its present implementation, parallelization is achieved by dividing the flow domain in subdomains that communicate their boundary values. For simplicity, the domain decomposition is 1-D: the tank has been divided in axial slices. If, on a homogeneous computer cluster, the slices have equal size, the computational load for solving the single-phase flow is properly balanced.

The presence of particles in the stirred tank significantly complicates parallelization of the computer code. In the first place, load-balancing needs to be reconsidered since the computational load of a subdomain now depends in a quite unpredictable manner on the number of particles inside the subdomain: local regions of high particle concentration within a subdomain draw heavily on the collision algorithm. Since the particle concentration field is not known *a priori*, the computational load per subdomain is unknown and fluctuating. Furthermore, there is much more communication between subdomains compared to a (single-phase) lattice-Boltzmann simulation: once particles cross a subdomain border, they must be transferred to the neighboring domain. Moreover, the velocity interpolation to determine the drag forces on particles and the calculation of stress gradients require the exchange of extra continuous phase flow information at subdomain borders. For the handling of particle-particle collisions in the vicinity of subdomain borders, not only the particles that cross the borders, but also particles close to the borders, need to be communicated.

Static load balancing has been applied in the Eu/La computer code. A simulation starts by releasing the solid particles homogeneously in a fully developed single-phase flow field. Once a more or less steady distribution of solid particles in axial (that is, vertical) direction was achieved, the subdomain sizes were adapted in such a way that the load was properly balanced. This load-balancing strategy is only successful if all communication actions that occur every time step are concentrated to one moment in the time-stepping algorithm, as has been done in our implementation. If the different parts of the code (continuous phase fluid dynamics, particle motion, collisions) have their own communication routines, much CPU time is wasted in waiting for neighboring subdomain information.

Overview of the simulation cases

In the Flow System section, two sets of particles have been defined. Particle set No. 1 was used in four simulations, and particle set No. 2 in two.

In simulation No. 1A, the particles only experience drag, gravity, and added mass. In simulation No. 1B, the set of forces is extended with the Saffman, Magnus, and stress-gradient force. For this reason, the equation of angular motion (Eq. 7) is included. Particle-particle collisions are introduced in simulation No. 1C. Finally, in simulation No. 1D two-way coupling is switched on.

Two simulations with particle set No. 2 have been performed: In No. 2A the full equation of motion (that is, Eq. 3) is solved, and particle-particle collisions are taken into account, but two-way coupling is discarded. In simulation No. 2B two-way coupling is switched on.

The set of simulated cases is summarized in Table 1. The time-averaged results that will be presented were obtained by running the simulations over a certain number of impeller revolutions, which is indicated in the last column of Table 1.

Results

Velocity and particle distributions

Overall impressions of the flow field, and the distribution of particles are given in Figures 2 and 3, respectively. In Figure 2, an instantaneous realization of the flow in the vertical plane midway between two baffles is compared to the time-averaged flow. This figure illustrates the relevance of performing time-dependent flow simulations with a view to particle tracking. For a particle released in the tank, the average flow is an artifact: the particle will feel the eddy-like, erratic structures in the instantaneous flow field, not the smooth average field. Furthermore, heat and mass transfer between solid and liquid is likely to be controlled by the fluctuations, rather than by the average flow. The single realization of the particle distribution in two cross sections in the tank (Figure 3) shows some peculiar features. In the horizontal cross section, large voids behind, and high solids concentrations in front of, the blades are observed. As a result, high particle-impeller collision frequencies can be anticipated. The streaks of particles that are shed from the blades keep their identity over quite a radial distance and give rise to high phase-averaged particle concentrations at the impeller level outside the impeller swept volume. Centrifugal forces induce high solids concentrations in the vicinity of the tank's outer wall. The vertical section shows particles throughout the tank, organized in streaky patterns. The concentrations are high at the bottom and outer wall. The upwardly flowing region underneath the impeller carries highly concentrated slurry towards

Table 1. Overview of Simulated Cases

Case No.	Particle Dia.	N (N_{js}) rev/s	$\boldsymbol{F}_{\text{Magnus, Saffman, stress}}$	*p-p* collisions	Particle-Fluid Coupling	Duration
1A	$d_p = 0.3$ mm	16.5 (13)	no	no	1-way	10 rev
1B	$d_p = 0.3$ mm	16.5 (13)	yes	no	1-way	12 rev
1C	$d_p = 0.3$ mm	16.5 (13)	yes	yes	1-way	20 rev
1D	$d_p = 0.3$ mm	16.5 (13)	yes	yes	2-way	20 rev
2A	$d_p = 0.468$ mm	25 (17)	yes	yes	1-way	20 rev
2B	$d_p = 0.468$ mm	25 (17)	yes	yes	2-way	20 rev

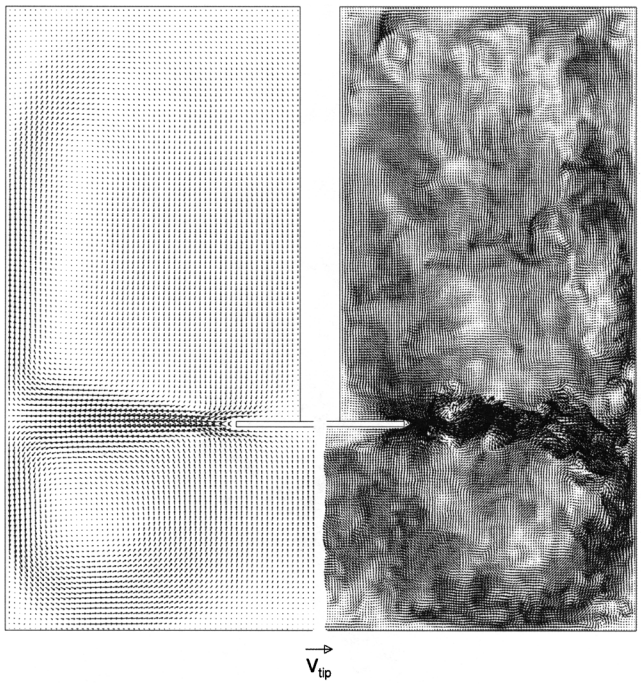

Figure 2. Velocity vector field at $Re = 1 \cdot 10^5$ in the vertical plane, midway between two baffles.

(Left) phase-averaged flow in half of the spatial resolution; (right) snapshot at the full resolution. One-way coupled simulation (case No. 1C), that is, the solid particles did not influence the flow field.

the impeller. The region void of particles extending from the bottom to closely underneath the impeller slightly left from the tank's centerline is the manifestation of a slowly precessing vortex that, at the moment the snapshot was taken, crossed the vertical cross section. The locally high vorticity inhibits the presence of particles. The precessing vortex is a manifestation of a macroinstability in the stirred tank (Nikiforaki et al., 2003).

In Figure 4, grid and SGS velocity magnitudes are compared. As can be observed, the SGS velocities are at least one order of magnitude lower than the grid-scale velocities. As a consequence, it is anticipated that the resolved velocity field dominates particle motion. Note also that, in the wake of the impeller blades, the magnitude of the resolved velocity exceeds the impeller tip speed.

One-way coupling

In this section, the simulations No. 1A, No. 1B, and No. 1C will be compared in terms of the time-average, vertical distribution of the particles in the tank. The particle number concentrations presented here have a spatial resolution of one lattice-Boltzmann grid-cell. They were determined by increasing a grid-cell counter with the number of particles present in that grid-cell each time step. The concentration profiles presented are steady-state profiles. After homogeneously introducing the particles in a fully developed flow, it took some 20–30 impeller revolutions for the particle system to become (quasi) steady. This process was monitored by keeping track of the number of particles in each subdomain

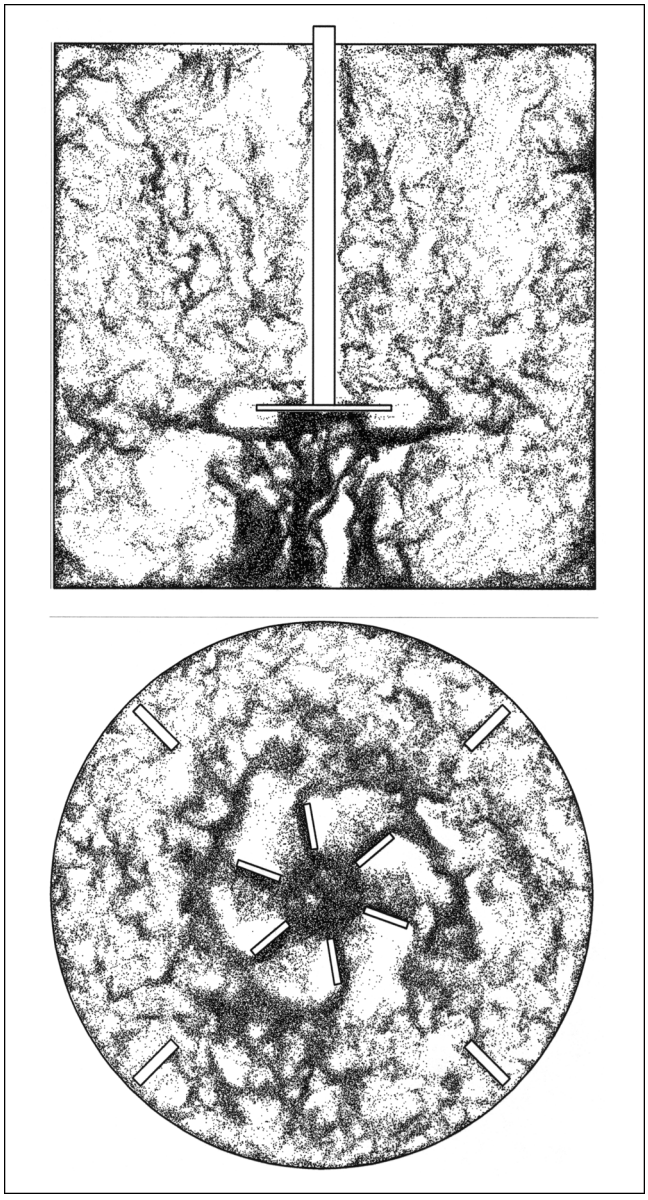

Figure 3. Instantaneous realization of the particle distribution in the tank for case No. 2B.

(Top) vertical cross section through the center of the tank midway between two baffles; (bottom) horizontal cross section at $z/T = 0.308$ (that is, just below the impeller disk). The impeller rotates in the counter-clockwise direction. In both graphs, the particles in a slice with thickness $0.0083T$ have been displayed.

(in the section on *parallelization* it was explained that these are horizontal slices in the tank). A good insight in the development of the vertical concentration profile was obtained this way. In the three simulations discussed here, particle and fluid motion was one-way coupled.

Gravity and the presence of the impeller induce strongly pronounced particle number concentration profiles (see Figure 5): in the impeller stream and close to the bottom the particle concentration is high. Above the impeller, more or less uniform concentrations (slightly lower than the tank-average concentration) are encountered. This global picture

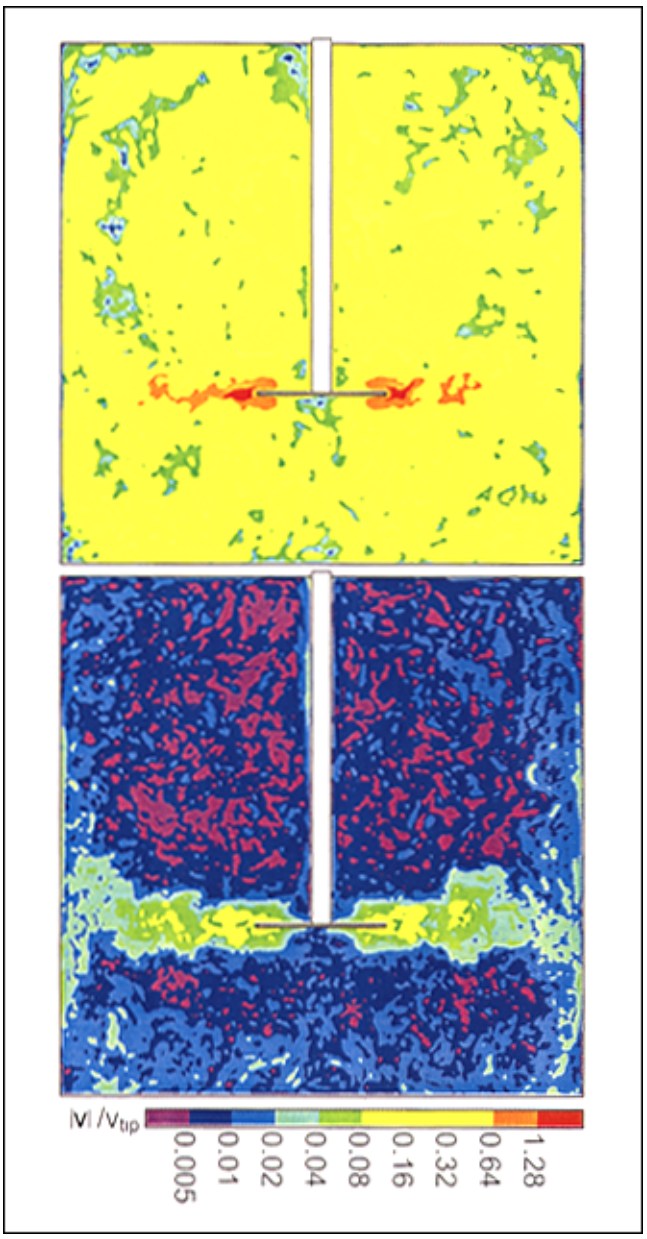

Figure 4. Instantaneous realization of the velocity field in a vertical cross section midway between two baffles in terms of contours of the velocity magnitude (case No. 1C).

(Top) magnitude of the resolved velocity; (bottom) magnitude of the subgrid-scale velocity $u_{sgs} = \sqrt{2/3 k_{sgs}}$ with k_{sgs} estimated with Eq. 8. Note the logarithmic color scale.

qualitatively corresponds to experimental data obtained in similar liquid-solid systems (Micheletti et al., 2003). The absence/presence of the Saffman, Magnus, and stress-gradient forces has no significant impact on the concentration profiles; the profiles of case No. 1A and No. 1B are the same within the bounds of statistical fluctuations. Switching on the particle-particle collisions, however, has dramatic impact. In the first place, the concentration peaks at the impeller level (at $z/D = 0$) become much higher. In the second place (and this cannot be judged clearly from Figure 5), the concentrations close to the bottom decrease significantly. At the radial position $2r/T = 0.3$, the time-averaged particle concentration in the first grid-cell above the bottom was 88, 71, and 21 times c_{av} for cases No. 1A, No. 1B, and No. 1C, respectively. The former two values (88 and 71) indicate physically unrealistic volume fractions of 84 and 67%, respectively (that is, close to or even higher than a closest packing of spheres which contains 74% of solids). The exclusion effect brought about by the particle-particle collision algorithm reduces the volume fractions in the bottom grid-cells to realistic proportions.

One-way coupling vs. two-way coupling

The presence of solid particles alters the turbulent flow field in the tank. The strongest influence of the particles is felt in the impeller stream: the slip velocities are highest here due to vigorous turbulent motion on the one hand and particle inertia on the other. The ratio between the particle relaxation time and the time between two blade passages equals six times (there are six impeller blades) the Stokes number (as defined in the Flow System section). For the two particle sets considered here, this ratio is of the order of unity, and, as a result, the particles are given insufficient time to relax to the local flow field before another impeller blade passes by. The high slip velocities induce appreciable momentum exchange between solid and liquid, which alters the local flow field.

Figure 6 displays the phase-averaged impeller outstream profiles for one-way and two-way coupled cases of the tangential, and radial velocity, as well as of the turbulent kinetic energy $k = 1/2(\overline{\langle u_i^2 \rangle_\theta} - \overline{\langle u_i \rangle_\theta^2})$, where the brackets $\langle\ \rangle_\theta$ indicate phase-resolved averages at impeller position θ and the overbar indicates averaging over all angular positions (the subscript i denotes the velocity components, and the summation convention has been applied). The impact of the particles on the k-levels close to the impeller is considerable: turbulence appears to be damped by the particles (this is also illustrated by Figure 7 which shows phase-averaged contours of k near the impeller with and without two-way coupling), even at the relatively low tank-average solids volume fraction of case No. 1D (0.95%). It is believed that the effect is so strong due to the locally high solids volume fractions in the vicinity of the impeller (typically four times the average solids volume fraction, see Figure 5, and also Figure 9). At $2r/D = 1.2$ and $2r/D = 1.5$, the particles make the k-profile much more asymmetric with respect to the impeller disk level. The asymmetry is due to the particle concentration being much higher underneath the disk than above the disk. The maximum tangential and radial phase-averaged velocity in the vicinity of the impeller tip is increased in the presence of particles due to particle inertia. At radial positions further away from the impeller (at $2r/D = 2.0$), all profiles more or less relax to the single-phase profiles. With regard to the liquid, the cases No. 1C and No. 2A are two single-phase flow cases with different Reynolds numbers ($Re = 1 \cdot 10^5$ and $Re = 1.5 \cdot 10^5$, respectively). Comparing them shows the limited impact the Reynolds number has on the profiles.

Investigating the phase-resolved average flow in the vicinity of the impeller reveals that the trailing vortex structure is changed by the particles. In the presence of particles, the

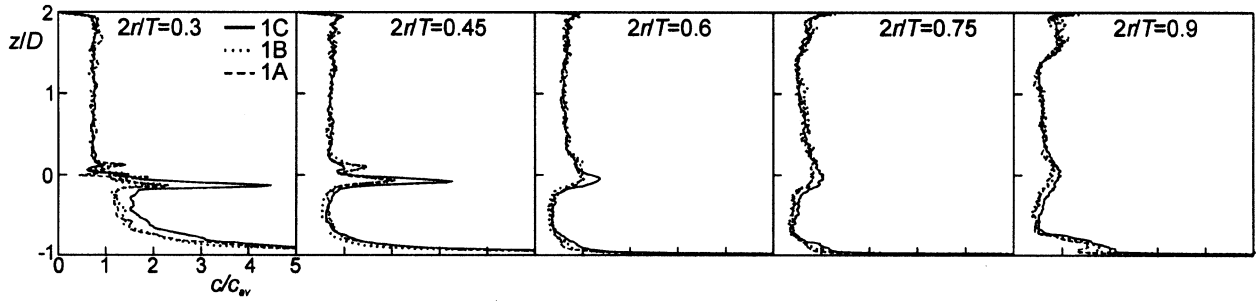

Figure 5. Phase-averaged particle number concentration in the plane midway between two baffles as a function of the vertical position in the tank at five different radial positions.

Comparison between cases No. 1A, No. 1B, and No. 1C, which all had $d_p = 0.30$ mm particles.

vortices appear to be slightly stretched in the radial direction as compared to their single-phase counterparts (Figure 8). Furthermore, the particles reduce the strength of the lower vortex, whereas the vorticity in the upper vortex increases. It has to be noted, however, that the two-way coupling effects (though significant) are not large. The relatively small changes in the flow field brought about by the particles are reflected in the particle concentration profiles: there are no large effects of two-way coupling here (see Figure 9). The particle concentrations close to the bottom are slightly reduced as a result of two-way coupling: at $2r/T = 0.45$, the concentrations relative to c_{av} in the first lattice cell for the simulations No. 1C and No. 1D are 18.5 and 16.3, respectively, and, for No. 2A and No. 2B, 6.66 and 6.15. The cases with the bigger particles (No. 2A and No. 2B) show more pronounced concentration profiles at the level of the impeller (please note the different concentration scale between the top and bottom of Figure 9).

Particle concentration fields

From now on, only simulations No. 1D and No. 2B will be discussed, since they represent the most complete physical picture. The way the particles are dispersed throughout the tank is shown in Figure 10. The particle number concentra-

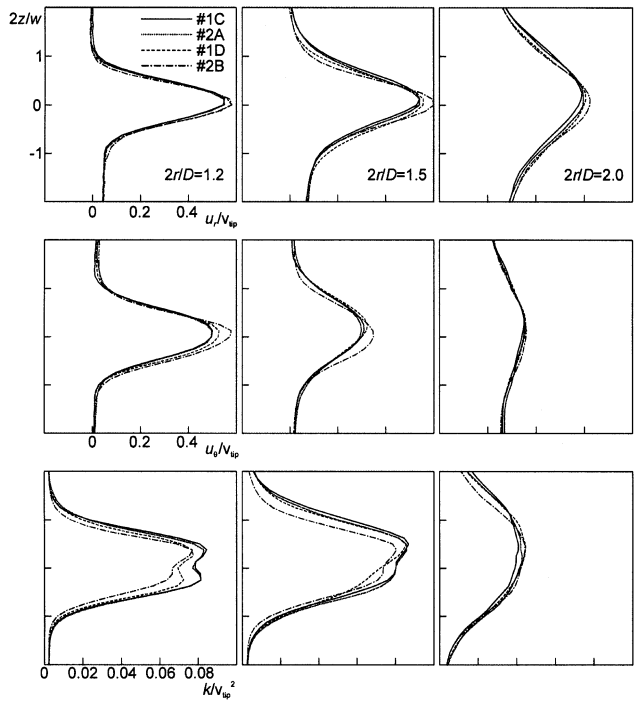

Figure 6. Phase-averaged impeller outstream profiles in the plane midway between two baffles at (from left to right) three radial positions.

Cases No. 1C, No. 2A, No. 1D, and No. 2B have been considered. From top to bottom: radial velocity, tangential velocity, and turbulent kinetic energy.

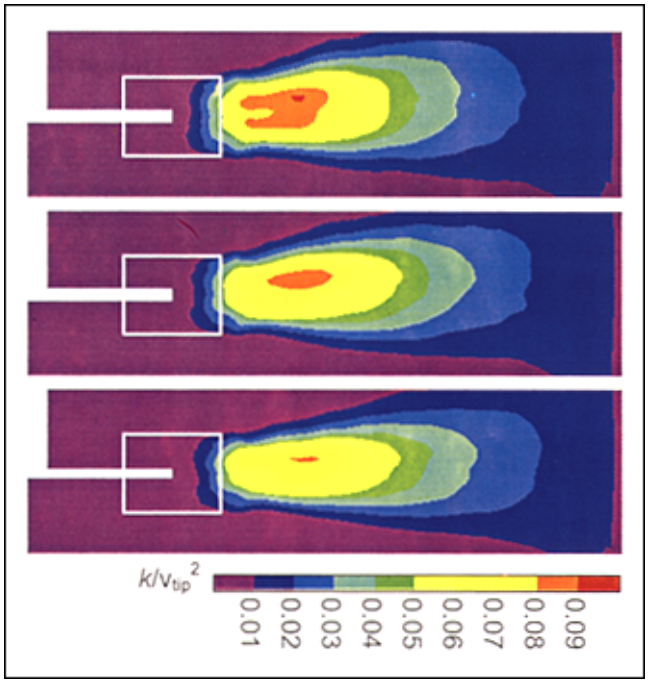

Figure 7. Phase-averaged contours of the turbulent kinetic energy in the vertical plane midway between two baffles in the vicinity of the impeller (the zero-angle blade position has been indicated by the white rectangle).

From top to bottom: case No. 1C (one-way coupled), No. 1D (two-way coupled, $\Phi_V = 0.95\%$), and No. 2B (two-way coupled, $\Phi_V = 3.6\%$).

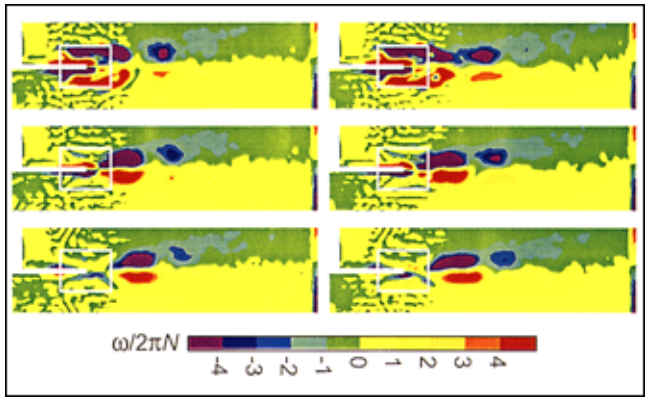

Figure 8. Phase-resolved contours of the vorticity in the direction normal to the plane of view in the vertical plane midway between two baffles.

(Left) case No. 1C (one-way coupled); (right) case No. 2B (two-way coupled, $\Phi_V = 3.6\%$). From top to bottom: 15°, 30°, and 45° behind the impeller blade. The white rectangle indicates the impeller blade in the zero-angle position.

tions are above average close to the bottom, underneath the impeller, in the lower half of the impeller stream, and close to the outer wall. The high concentrations underneath the impeller are due to the long residence times there. The (downward) settling velocity and the upward fluid motion give rise to low particle velocities in absolute terms. The sharply peaked concentrations slightly below disk level are due to the accumulation of particles in front of the impeller blades, and due to the streaks of particles that are continuously being shed from the blades, as already witnessed in Figure 3. The radial extent of the peak concentrations closely underneath disk level corresponds to the radial position where the disintegration of the streaks in the highly turbulent impeller stream starts. The high concentrations in a thin layer at the outer tank wall are due to centrifugal forces induced by the swirl induced by the impeller. The vicinity of the point where the

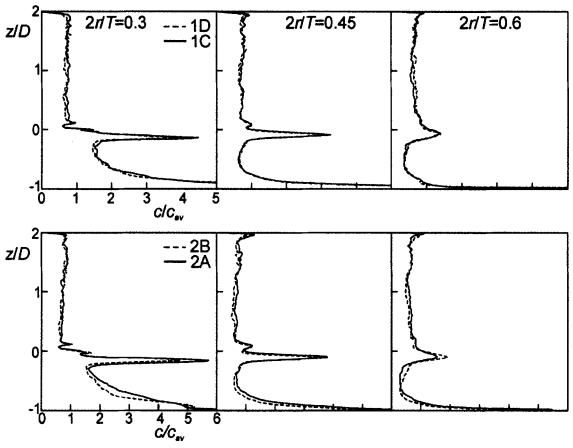

Figure 9. Phase-averaged particle concentration in the plane midway between two baffles as a function of the vertical position in the tank at three different radial positions.

Comparison between one-way (No. 1C and No. 2A), and two-way (No. 1D and No. 2B) coupled cases.

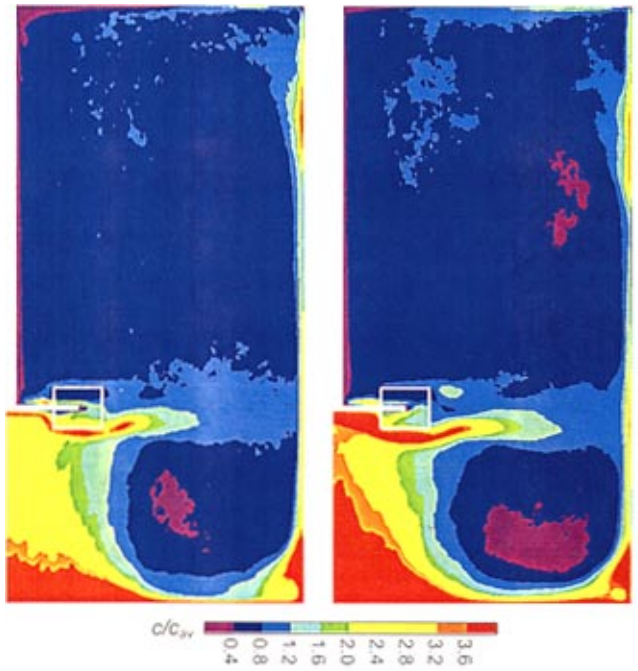

Figure 10. Phase-averaged particle concentration contours in the vertical plane midway between two baffles.

(Left) case No. 1D; (right) case No. 2B.

upper recirculation loop separates from the tank wall (see the left part of Figure 2) is also characterized by high particle concentrations. The downward shift of this point in case No. 2B compared to No. 1D reflects a solid-particle holdup effect.

Phase-resolved concentration contours in the vicinity of the impeller (Figure 11) give a quantitative view of the regions void of particles in the wake of the impeller blades, and the accumulation of particles in front of the blades (the 55° position). The void is advected radially into the bulk of the tank at a pace similar to the upper vortex (compare Figure 11 with Figure 8). The lower vortex contains many particles, which probably is the reason that its strength (in terms of the vorticity) is reduced by the presence of the particles. Due to the higher inertia of the bigger particles, the high particle concentration region at disk level extends over a larger radial distance.

A preliminary assessment of the solids concentration distribution by means of experimental data is shown in Figure 12. For this purpose, measurements due to Micheletti et al. (2003) have been used. Among the many cases they investigated, one was relatively close to the conditions of case No. 2B: glass beads with d_p between 0.3 and 0.425 mm at $\Phi_V = 5.5\%$ in a baffled tank ($T = 0.290$ m) with a Rushton turbine revolving at N_{js}. The peak concentration at $z/D \approx 0.0$ is well represented by the simulations. In the bulk of the tank, however, the solids concentration is systematically underpredicted. More experimental data (at more positions in the tank, and preferably phase-resolved) and a closer match between numerical and experimental conditions are required to draw firm conclusions with respect to confidence levels of the modeling effort.

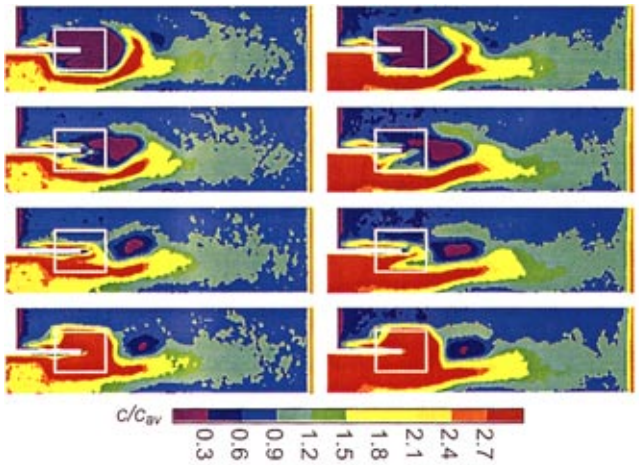

Figure 11. Phase-resolved particle concentration fields in a vertical plane midway between two baffles in the vicinity of the impeller (the white rectangle indicates the position of the impeller blade in the zero-angle position).

(Left) case No. 1D; (right) case No. 2B. From top to bottom: 15°, 30°, 45°, and 55° behind the impeller blade.

Collisions

In this section, two types of collisions will be considered: particle-particle and particle-impeller collisions. Collisions in turbulently agitated solid-liquid systems are highly relevant. Particle breakage is considered to be the result of particles colliding with one another, or with the internals of the reactor. In industrial crystallization, breakage of particles is a main source of secondary nucleation, and, therefore, strongly influences product quality (such as in terms of the crystal-size distribution). In catalytic slurry reactors, wear of the solids is a significant problem, since it degrades the catalytic material and makes separation steps (fines removal) necessary.

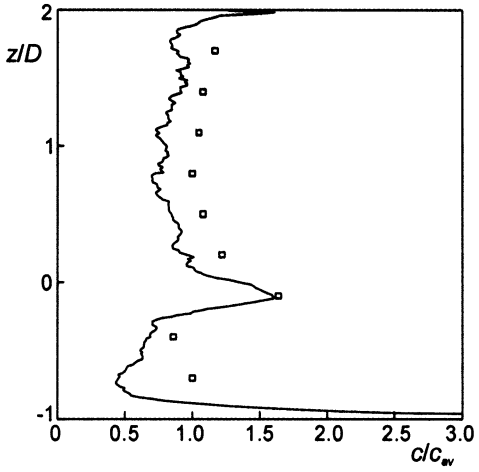

Figure 12. Phase-averaged particle concentration in the plane midway between two baffles as a function of the vertical position in the tank at $2t/T = 0.7$ for case No. 2B (drawn line), and for experiments reported by Micheletti et al. (2003) with glass beads in the size range 0.3–0.425 mm (symbols).

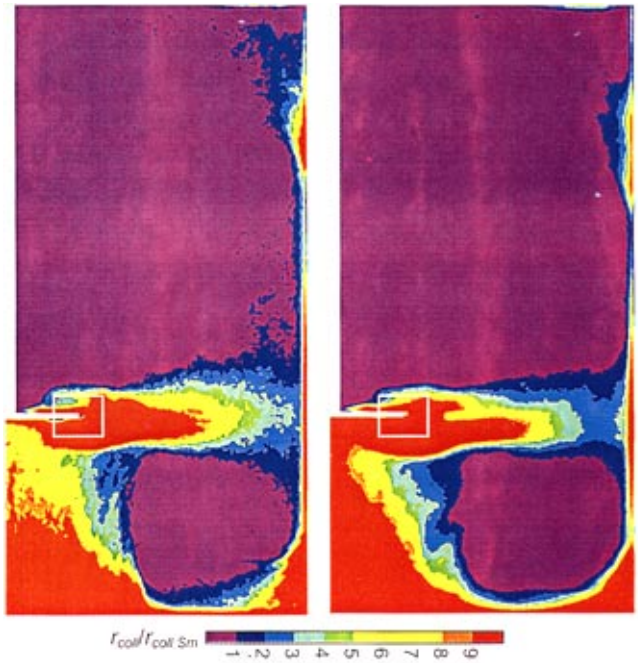

Figure 13. Phase-averaged contours of the particle-particle collision rate in the vertical plane midway between two baffles.

(Left) case No. 1D; (right) case No. 2B. The collision rate has been normalized with the Von Smulochowski collision rate $r_{\mathrm{coll},Sm}$ (Eq. 11).

In the simulations, the particle-particle collisions were carried out explicitly. For statistical processing, we have stored the characteristics of the particle-particle collision events taking place in a set of pre-selected planes in the tank. In this article, results in the vertical plane midway between two baffles will be presented. In order to usefully compare the two cases, we non-dimensionalized the observed collision rate with the collision rate from the Von Smulochowski (1917) relation for particle collisions in shear flow

$$r_{\mathrm{col},Sm} = \frac{4}{3}\gamma d_p^3 c_{av}^2 \tag{11}$$

For the shear rate γ, a tank-average value based on the tank-average dissipation rate $\bar{\epsilon}$ has been applied: $\gamma = \sqrt{\bar{\epsilon}/\nu}$. The tank average dissipation rate amounts to $\bar{\epsilon} = PoN^3D^5/V_{\mathrm{tank}}$ with $Po = 5.0$ the power number for a Rushton turbine revolving in a baffled tank (Rushton et al., 1950), and V_{tank} the volume of the tank. The phase-averaged results are shown in Figure 13. The two contour plots look quite similar, demonstrating that the normalization with the Von Smulochowski relation is a fair way to scale the system in terms of collision rates. Since Eq. 11 contains the particle size d_p to the power three, whereas the average dissipation rates scales like $\bar{\epsilon} \propto N^3$, in absolute terms the collision rate in case No. 2B is about seven times the rate in case No. 1D.

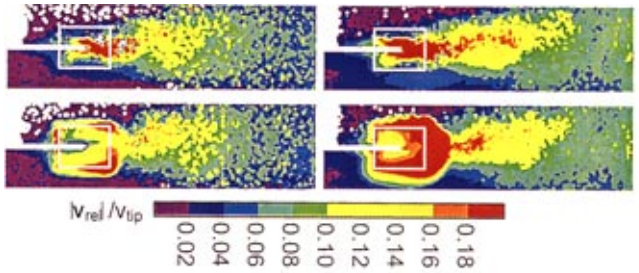

Figure 14. Phase-resolved contours of the relative velocity with which two particles collide in the vertical plane midway between two baffles in the vicinity of the impeller.

(Left) case No. 1D; (right) case No. 2B. (Top) 30° behind the impeller blade; (bottom) 55°.

As explained above (in the section on the way the particle-particle collisions are computationally handled), a particle is allowed to only collide once during one time step. This inevitably will lead to situations in which some collisions are missed. The number of times that the missed-collision-algorithm was executed has been compared to the number of proper collisions. For case No. 1D, the number of missed collisions was less than 2% of the number of proper collisions everywhere in the tank. For case No. 2B, relatively more collisions were missed: on average 9%, with peak values of 80% directly in front of the impeller blades. This is due to the significantly higher solids loading in case No. 2B. The number of missed collisions can be reduced (in principle to any desired level) by reducing the time step of the particle motion algorithm, that is, at the expense of computer time.

With a view to the mechanical load on the particles, not only the collision frequency, but also the relative velocities with which the particles collide is relevant. Obviously, these are highest in the impeller swept region and in the impeller stream. The collision intensities have been quantified in Figure 14. As can be seen, relative velocities between particles higher than 18% of the impeller tip speed are no exception. Due to their higher inertia, the bigger particles (No. 2B) collide with greater relative velocities than the smaller particles (No. 1D). The white dots in Figure 14 indicate that, during the course of the simulation, no collision occurred in that specific grid cell, at that specific impeller position.

It is interesting to compare the frequencies and intensities of particle-particle collisions with those of particle-impeller collisions, such as in order to estimate which type of collision is most responsible for attrition. In Figure 15a, the collision rate per unit blade area has been non-dimensionalized with

$$r_{\text{blade},0} = \frac{c_{av} V_{\text{blade}} N}{A_{\text{blade}}} \tag{12}$$

which is the number of particles in the blade swept volume V_{blade} ($V_{\text{blade}} = 0.2D(\pi/4)\ (D^2 - (0.5D)^2)$ in the case of a uniform particle concentration in the tank (c_{av}) times the impeller speed N, divided by the total impeller blade front-surface A_{blade} ($A_{\text{blade}} = 6 \cdot 0.2D \cdot 0.25D$; there are 6 impeller blades). The distribution of collision rates over the front surface of the impeller blade reflects the inhomogeneity of the particle concentration in front of the blade. At the lower portion of the blades (with higher particle concentrations due to the highly concentrated upwardly directed flow underneath the impeller), much higher collision rates are encountered than higher up at the blade. This qualitatively corresponds to experimental findings by Kee and Rielly (2000). If we integrate the total number of particle-impeller collisions, in case No. 1D a particle, on average, hits the front of the impeller blade 0.11 times per impeller revolution; in case No. 2B, the value is 0.21, that is, significantly higher. The number of particle-particle collisions is much larger: in case No. 1D, a particle, on average, collides 5.1 times during one impeller evolution with another particle; in case No. 2B, even 14.1 times.

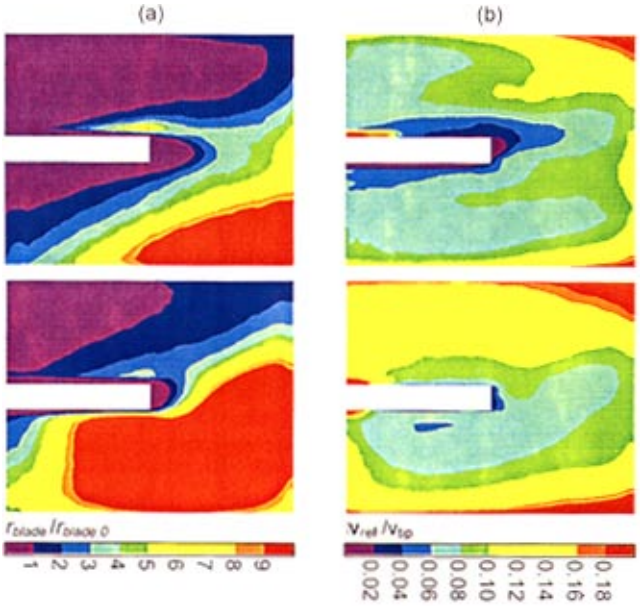

Figure 15. Contours on the front surface of the impeller blade.

(Top part) case No. 1D; (bottom part) case No. 2B. (a) Phase-averaged blade-particle collision rate per unit area (r_{blade}), normalized with $r_{\text{blade},0}$ (see Eq. 12); (b) average relative velocity at a blade-particle collision.

At the upper and lower blade edges, the intensity of the particle-impeller collisions is highest (see Figure 15b). It is remarkable to see that, at the blade tip, the impact velocities are relatively low. We speculate that this is due to the predominantly radially directed flow at the blade tip that helps particles escape from the blade, whereas the flow above and below the blade is predominantly towards the blade. Relative velocities at particle-particle and particle-impeller blade collisions are quite comparable.

The data stored with respect to the particle-impeller collisions allowed the determination of the probability density function (pdf) of the impact velocity. Approximately exponential pdf's were obtained (see Figure 16). The chances of high impact velocities (as high as the impeller tip speed) significantly increase with increasing particle size.

The momentum exchange between the solid particles and the impeller (Eq. 10) gives rise to an additional torque. For case No. 1D, the torque directly related to particle-impeller

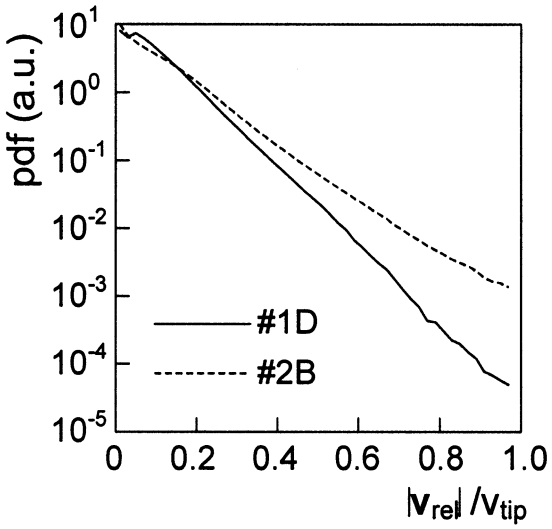

Figure 16. Probability density function of the relative velocity at particle-blade impact.

collisions was 2.3% of the torque exerted on the fluid. The latter torque had increased with 2.5% compared to the torque in a one-way coupled simulation at the same impeller speed. As a result, the total torque increased with some 5%. For case No. 2B, the equivalent values were 11% for the torque due to particle-impeller collisions, and 4% for the torque exerted on the fluid, with the overall value being 15%. The overall values are higher (by a factor of approximately 1.5) compared to power measurements in similar flow systems reported by Micheletti et al. (2002).

Linear and rotational slip velocities

Finally, the spatial distribution of the slip velocities will be considered. Their relevance lies in heat and mass transfer between solid and liquid. The results will be presented in terms of particle Reynolds numbers. We not only consider here the Reynolds number related to the linear slip velocity Re_p, but also the Reynolds number related to the rotational slip velocity Re_R. The velocity scale for both Reynolds numbers is the relative velocity of the solid surface with respect to the fluid in its direct surroundings. Therefore, if the two Reynolds numbers are of comparable magnitude, translation and rotation may contribute comparably to the overall mass-transfer coefficient. The largest particle Reynolds numbers can be found in the impeller swept region and in the impeller outstream (see Figure 17). The case with the smaller particles (No. 1D) has rotational Reynolds numbers that are one order of magnitude smaller than translational Reynolds numbers. For the case with the bigger particles (No. 2B), the two Reynolds numbers are much closer and it is expected that rotation adds appreciably to the solid-liquid mass transfer. It has to be noted, however, that, for case No. 2B, rotational Reynolds numbers in the impeller region exceed the range of applicability of Eq. 7.

Conclusions

Two-phase (solid-liquid) simulations of the turbulent flow in a stirred tank according to an Eulerian/Lagrangian approach have been presented. In this approach, a large number (6.7 million) of particles was tracked in a liquid flow field that was represented by a large-eddy simulation (LES). The grid used in the LES was sufficiently fine in order to have little turbulent kinetic energy residing at subgrid-scales. It was demonstrated that, due to the small time step and the fine spatial grid, the particles mainly felt the resolved flow scales. Albeit of little influence, the action of the SGS flow on the particles was mimicked by means of a stochastic process. The hydrodynamic forces acting on the particle that were considered in this article were nonlinear drag, the force related to

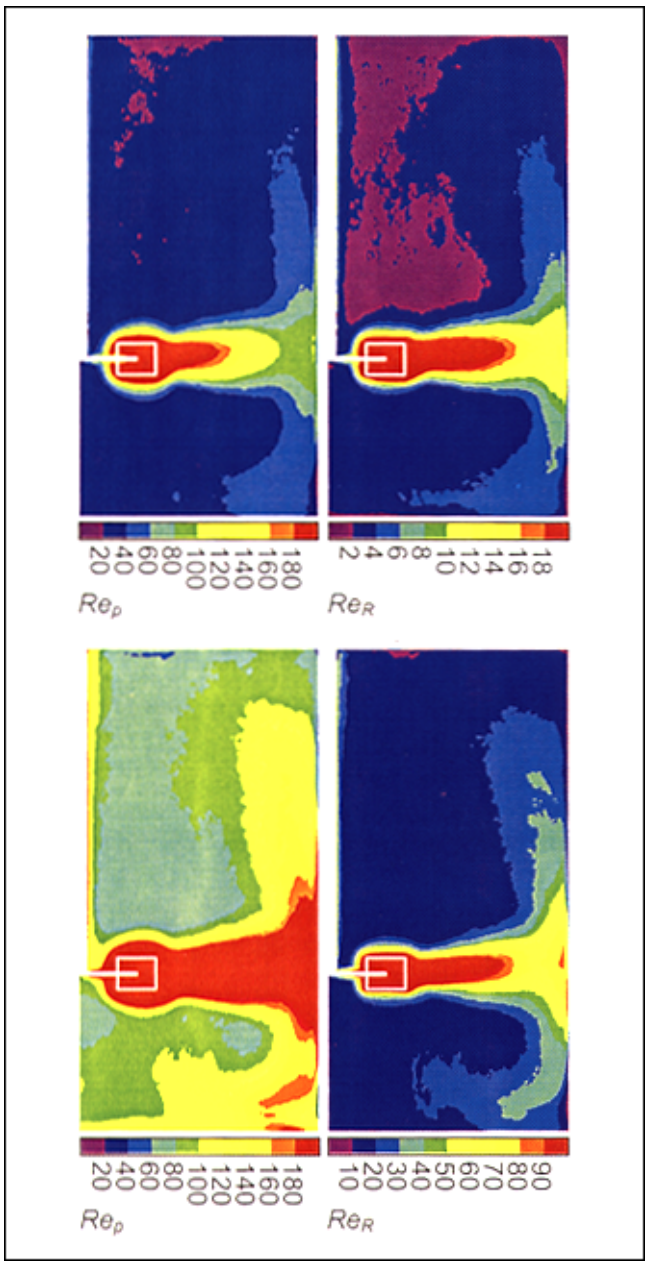

Figure 17. Phase-averaged distributions of the linear and rotational Reynolds numbers (Re_p and Re_R, respectively) in a vertical plane midway between two baffles.

(Top) case No. 1D; (bottom) case No. 2B.

added mass, lift forces (Saffman and Magnus force), and forces due to stress gradients. The Basset history force has been neglected for physical, but also for computational, reasons.

The simulations show some typical features with respect to the distribution of solids in the tank. The particles organize in streaky patterns, thereby avoiding high-vorticity regions. These streaks develop irrespective of one- or two-way coupling between fluid and solids. The region underneath the Rushton turbine carries a highly concentrated slurry towards the impeller. In front of the impeller blades, particles accumulate; behind the impeller blades, large volumes void of particles are formed. The net effect is a peak in the phase-averaged particle concentration at the axial level of the impeller.

The just-suspended criterion (Zwietering, 1958) proved to be a crucial test for the assumptions related to solid particle modeling. Simulations with impeller speeds clearly above N_{js} with only drag and added mass as the hydrodynamic forces showed unphysically high solids concentrations closely above the bottom. Adding the lift and stress gradient forces showed no improvement. Only when particle-particle collisions were taken into account, a realistic particle distribution throughout the tank was obtained. This improvement was primarily caused by the exclusion effect brought about by the collision algorithm: the algorithm inhibits particles to be at mutual distances smaller than the particle diameter.

The simulations gave detailed, quantitative insight in the particle behavior in the tank: phase-averaged and phase-resolved particle concentration fields; linear and rotational slip velocities; and data on collisions. The intensity of particle-particle and particle-impeller collisions (in terms of the relative velocity at impact) proved to be quite comparable. For the specific flow systems studied in this article, however, the number of particle-particle collisions was much higher than the number of particle-impeller collisions. For the bigger particles, it was demonstrated that particle rotation might significantly add to mass-transfer coefficients.

There is quite some room for improvement with respect to the modeling attempt presented here. In the first place, the simulations with the bigger particles (notably case No. 2B with $d_p = 0.468$ mm) went beyond the ranges of applicability with respect to the particle angular velocities, and with respect to the time step in relation to the particle-particle collision algorithm (too many missed collisions). In the second place, the hydrodynamic forces were based on single-particle correlations; hydrodynamic interactions between particles were not taken into account. The former issues can easily be repaired by adapting the coefficients in the dynamic equation for particle rotation, and by reducing the time step. A first step with respect to the latter issue would be the inclusion of a drag coefficient that not only depends on the particle Reynolds number, but also on the local solids volume fraction (see, for example, Crowe et al., 1998). A more advanced approach could be based on direct numerical simulations at the scale of the particles in simple geometries where relations for hydrodynamic interaction forces could be derived that take into account the topology of particle clusters.

The simulations discussed here qualitatively agree with the experimental data available so far: the particles indeed get suspended above N_{js}; the peak in the axial, phase-averaged particle concentration profile at the level of the impeller has been observed experimentally; the distribution of the particle-impeller collisions over the blade surface corresponds to experiments by Kee and Rielly (2000). However, a preliminary comparison between one vertical concentration profile in one of our simulations with an experimental profile (Micheletti et al., 2003) points to an underestimation of the solids bulk-concentration. Detailed experiments are needed to further assess the confidence level of the simulations discussed in this article. These experiments should comprise particle concentration fields, preferably phase-resolved and in the vicinity of the impeller, more experiments on particle-impeller collisions such as presented by Kee and Rielly (2000), and nonintrusive experiments on the liquid-phase flow velocities in the presence of particles. The latter are especially very intricate, because without special measures such as refractive index matching, the optical accessibility of the flow system is limited to the region close to the outer wall.

Acknowledgment

The author acknowledges support by the EU under the Growth Programme project Optimization of Industrial Multiphase Mixing (G1RD-CT-2000-00263).

Literature Cited

Baldi, G., R. Conti, and E. Alaria, "Complete Suspension of Particles in Mechanically Agitated Vessels," *Chem. Eng. Sci.*, **33**, 21 (1978).

Chen, M., K. Kontomaris, and J. B. McLaughlin, "Direct Numerical Simulation of Droplet Collisions in a Turbulent Channel Flow. Part I: Collision Algorithm," *Int. J. Multiphase Flow*, **24**, 1079 (1998).

Chen, S., and G. D. Doolen, "Lattice Boltzmann Method for Fluid Flows," *Annu. Rev. Fluid Mech.*, **30**, 329 (1998).

Crowe, C. T., T. R. Troutt, and J. N. Chung, "Numerical Models for Two-Phase Turbulent Flows," *Ann. Rev. Fluid Mech.*, **28**, 11 (1996).

Crowe, C., M. Sommerfeld, and Y. Tsuji, *Multiphase Flows with Droplets and Particles*, CRC Press, Boca Raton, FL (1998).

Dennis, S. C. R., S. N. Singh, and D. B. Ingham, "The Steady Flow Due to Rotating Sphere at Low and Moderate Reynolds Numbers," *J. Fluid. Mech.*, **101**, 257 (1980).

Derksen, J. J., and H. E. A. van den Akker, "Parallel Simulation of Turbulent Fluid Flow in a Mixing Tank," *Lect. Notes Computer Sci.*, **1401**, 96 (1998).

Derksen, J. J., and H. E. A. Van den Akker, "Large Eddy Simulations on the Flow Driven by a Rushton Turbine," *AIChE J.*, **45**(2), 209 (1999).

Derksen, J., "Assessment of Large Eddy Simulations for Agitated Flows," *Trans. IChemE*, **79A**, 824 (2001).

Elgobashi, S., "On Predicting Particle-Laden Turbulent Flows," *Appl. Sci. Res.*, **52**, 309 (1994).

Hollander, E. D., J. J. Derksen, L. M. Portela, and H. E. A. van den Akker, "Numerical Scale-up Study for Orthokinetic Agglomeration in Stirred Vessels," *AIChE J.*, **47**(11), 2425 (2001).

Kee, K. C., and C. D. Rielly, "An Experimental Method for Obtaining Particle Impact Frequencies and Velocities on Impeller Blades," *Proc. of 10th European Conf. on Mixing*, 213, Delft, Netherlands, Elsevier, Amsterdam (2000).

Kiparissidis, C., "Polymerization Reactor Modeling: A Review of Recent Developments and Future Directions," *Chem. Eng. Sci.*, **51**, 1637 (1996).

Lain, S., M. Sommerfeld, and J. Kussin, "Experimental Studies and Modelling of Four-Way Coupling in Particle-Laden Horizontal Channel Flow," *Int. J. Heat Fluid Flow*, **23**, 647 (2002).

Mason, P. J., and N. S. Callen, "On the Magnitude of the Subgrid-Scale Eddy Coefficient in Large-Eddy Simulations of Turbulent Channel Flow," *J. Fluid Mech.*, **162**, 439 (1986).

Maxey, M. R., and J. J. Riley, "Equation of Motion for a Small Rigid Sphere in a Nonuniform Flow," *Phys. Fluids*, **26**, 883 (1983).

Mei, R., "An Approximate Expression for the Shear Lift Force on a Spherical Particle at Finite Reynolds Numbers," *Int. J. Multiphase Flow*, **18**, 145 (1992).
Micheletti, L., L. Nikiforaki, K. C. Lee, and M. Yianeeskis, "Integral and Local Concentration Characteristics of Moderate to Dense Solid-Liquid Suspensions," *11th European Conference on Mixing*, Bamberg, Germany in press (Oct. 2003).
Montante, G., G. Micale, F. Magelli, and A. Brucato, "Experiments and CFD Predictions of Solid Particle Distribution in a Vessel Agitated with Four Pitched Blade Turbines," *Chem. Eng. Res. Des.*, **79**, 1005 (2001).
Nikiforaki, L., G. Montante, K. C. Lee, and M. Yianneskis, "On the Origin, Frequency and Magnitude of Macro-Instabilities of the Flows in Stirred Vessels," *Chem. Eng. Sci.*, **58**(13), 2937 (July 2003).
Odar, F., and W. S. Hamilton, "Forces on a Sphere Accelerating in a Viscous Fluid," *J. Fluid Mech.*, **18**, 302 (1964).
Oesterlé, B. and T. Bui Dinh, "Experiments on the Lift of a Spinning Sphere in the Range of Intermediate Reynolds Numbers," *Exp. Fluids*, **25**, 16 (1998).
Rushton, J. H., E. W. Costich, and H. J. Everett, "Power Characteristics of Mixing Impeller I and II," *Chem. Eng. Prog.*, **46**, 395, 467 (1950).
Smagorinsky, J., "General Circulation Experiments with the Primitive Equations: 1. The Basic Experiment," *Mon. Weather Rev.*, **91**, 99 (1963).
Sommerfeld, M., "Validation of a Stochastic Lagrangian Modelling Approach for Inter-Particle Collisions in Homogeneous Isotropic Turbulence," *Int. J. Multiphase Flow*, **27**, 1829 (2001).
Von Smulochowski, M., "Versuch einer mathemischen Theorie der Koagulationkinetik koloider Lösungen," *Z. Phys. Chem.*, **92**, 156 (1917).
Weber, R., F. Boysan, W. H. Ayers, and J. Swithenbank, "Simulation of Dispersion of Heavy Particles in Confined Turbulent Flows," *AIChE J.*, **30**, 490 (1984).
Zwietering, Th. N., "Suspending of Solid Particles in Liquid by Agitators," *Chem. Eng. Sci.*, **8**, 244 (1958).

Appendix: Coefficients in Hydrodynamic Force Relations

Drag force

$$C_D = \frac{24}{Re_p}\left(1.0 + 0.15\,Re_p^{0.687}\right) \quad Re_p < 1{,}000$$

$$C_D = \quad 0.44 \quad\quad\quad\quad Re_p \geq 1{,}000 \qquad \text{(A1)}$$

Saffman force

$$C_S = \frac{4.1126}{Re_S^{0.5}}\left[\left(1.0 - 0.234\left(\frac{Re_S}{Re_p}\right)^{0.5}\right)e^{-0.1Re_p} + 0.234\left(\frac{Re_S}{Re_p}\right)^{0.5}\right] \qquad Re_p < 40$$

$$C_S = 0.1524 \qquad\qquad\qquad\qquad\qquad\qquad Re_p \geq 40 \qquad \text{(A2)}$$

Magnus force

$$C_M = 0.45 + \left(\frac{Re_R}{Re_p} - 0.45\right)e^{-0.05684\,Re_R^{0.4}Re_p^{0.3}} \qquad \text{(A3)}$$

Manuscript received Feb. 18, 2003, and revision received Apr. 15, 2003.